



HAL
open science

Methane Hydrate Formation and Dissociation in Sand Media: Effect of Water Saturation, Gas Flowrate and Particle Size

Fatima Doria Benmesbah, Livio Ruffine, Pascal Clain, Véronique Osswald, Olivia Fandino, Laurence Fournaison, Anthony Delahaye

► **To cite this version:**

Fatima Doria Benmesbah, Livio Ruffine, Pascal Clain, Véronique Osswald, Olivia Fandino, et al.. Methane Hydrate Formation and Dissociation in Sand Media: Effect of Water Saturation, Gas Flowrate and Particle Size. *Energies*, 2020, 13, 10.3390/en13195200 . hal-03171742

HAL Id: hal-03171742

<https://hal.inrae.fr/hal-03171742>

Submitted on 17 Mar 2021

HAL is a multi-disciplinary open access archive for the deposit and dissemination of scientific research documents, whether they are published or not. The documents may come from teaching and research institutions in France or abroad, or from public or private research centers.

L'archive ouverte pluridisciplinaire **HAL**, est destinée au dépôt et à la diffusion de documents scientifiques de niveau recherche, publiés ou non, émanant des établissements d'enseignement et de recherche français ou étrangers, des laboratoires publics ou privés.

Article

Methane Hydrate Formation and Dissociation in Sand Media: Effect of Water Saturation, Gas Flowrate and Particle Size

Fatima Doria Benmesbah ^{1,2,*}, Livio Ruffine ^{1,*} , Pascal Clain ^{2,3} , Véronique Osswald ² ,
Olivia Fandino ¹ , Laurence Fournaison ² and Anthony Delahaye ²

¹ Unité Géosciences Marines, Laboratoire Cycles Géochimiques (LCG), IFREMER, F-29280 Plouzané, France; olivia.fandino.torres@ifremer.fr

² INRAE, FRISE, Université Paris-Saclay, 92761 Antony, France; pascal.claifin@devinci.fr (P.C.); veronique.osswald@inrae.fr (V.O.); laurence.fournaison@inrae.fr (L.F.); anthony.delahaye@inrae.fr (A.D.)

³ Research Center, Léonard de Vinci Pôle Universitaire, 92916 Paris, France,

* Correspondence: fatima.benmesbah@inrae.fr (F.D.B.); livio.ruffine@ifremer.fr (L.R.)

Received: 6 July 2020; Accepted: 1 October 2020; Published: 6 October 2020



Abstract: Assessing the influence of key parameters governing the formation of hydrates and determining the capacity of the latter to store gaseous molecules is needed to improve our understanding of the role of natural gas hydrates in the oceanic methane cycle. Such knowledge will also support the development of new industrial processes and technologies such as those related to thermal energy storage. In this study, high-pressure laboratory methane hydrate formation and dissociation experiments were carried out in a sandy matrix at a temperature around 276.65 K. Methane was continuously injected at constant flowrate to allow hydrate formation over the course of the injection step. The influence of water saturation, methane injection flowrate and particle size on hydrate formation kinetics and methane storage capacity were investigated. Six water saturations (10.8%, 21.6%, 33%, 43.9%, 55% and 66.3%), three gas flowrates (29, 58 and 78 mLn·min⁻¹) and three classes of particle size (80–140, 315–450 and 80–450 μm) were tested, and the resulting data were tabulated. Overall, the measured induction time obtained at 53–57% water saturation has an average value of 58 ± 14 min minutes with clear discrepancies that express the stochastic nature of hydrate nucleation, and/or results from the heterogeneity in the porosity and permeability fields of the sandy core due to heterogeneous particles. Besides, the results emphasize a clear link between the gas injection flowrate and the induction time whatever the particle size and water saturation. An increase in the gas flowrate from 29 to 78 mLn·min⁻¹ is accompanied by a decrease in the induction time up to ~100 min (i.e., ~77% decrease). However, such clear behaviour is less conspicuous when varying either the particle size or the water saturation. Likewise, the volume of hydrate-bound methane increases with increasing water saturation. This study showed that water is not totally converted into hydrates and most of the calculated conversion ratios are around 74–84%, with the lowest value of 49.5% conversion at 54% of water saturation and the highest values of 97.8% for the lowest water saturation (10.8%). Comparison with similar experiments in the literature is also carried out herein.

Keywords: gas hydrate; porous media; kinetics; methane storage estimate; water saturation; gas flowrate; particle size

1. Introduction

Gas hydrates are non-stoichiometric crystalline structures made of water molecules forming a cavity, usually called a cage, in which lightweight gas molecules are enclathrated. They are stable under low-temperature and high-pressure conditions [1–3]. The most common enclathrated molecules

are light hydrocarbons, carbon dioxide, nitrogen and hydrogen sulfide. Earth's natural-gas hydrates are widespread on continental margin sediments as well as in permafrost, lakes and inland seas [4–9]. Enclathrated gases contain mainly methane of either thermogenic or microbial origin [8,10–13]; the most abundant hydrate-supplying methane source gases are microbial. Natural-gas hydrate deposits represent one of the largest methane reservoirs on earth [14,15]. Thus, it has been considered a potential energy resource, and intense studies are ongoing to both assess the amount of natural gas bound in these deposits and for the development of new technologies for future exploitation [16–22]. Natural-gas hydrates are very sensitive to changes in temperature, pressure and water chemistry (e.g., water salinity), and they are deemed to be a potential geohazard if one of these parameters evolves and triggers their destabilization [23–29].

Moreover, several hydrate-based industrial processes are under intense consideration with applications to gas separation, carbon dioxide capture and storage, water desalination as well as cold production and storage [1,3,5,30]. As an example, cold production and storage currently use harmful refrigerant materials such as chlorofluorocarbons (CFCs) and hydrofluorocarbons (HFCs), which directly impact global warming. To reduce this impact, hydrate-based secondary refrigeration using environmentally neutral secondary fluids [31–34] is under consideration an effective and promising solution.

One of the most advantageous properties of hydrates is their ability to store a large volume of gases. Previous studies have demonstrated that gas storage capacity and the hydrate formation rate are enhanced in porous media [35–37]. However, the influence of porous-media properties on hydrate formation kinetics and hydrate gas-storage capacity are still poorly understood. This conclusion also applies to other system parameters such as water saturation and the gas injection flowrate. Accordingly, to improve our knowledge of natural-gas hydrate dynamics, and the development of reliable hydrate-based industrial processes, intense investigations need to be pursued to: (1) clearly document and understand how key parameters affect hydrate formation and storage capacity, and (2) disentangle their relation to each other.

Previous studies showed that particle size can significantly influence the absolute and relative permeability of water and gases in porous media and hydrate saturation [26,38–41]. However, only a few studies show the influence of the sandy particle size on the induction time of methane hydrate formation: Prasad et al. [42] studied the effect of a suspension of 10 wt% silica particles (diameter 50, 150 and 200 μm) in pure water on induction time of methane hydrate. The induction times obtained are around 100, 70 and 60 min at silica particle size of 50, 150 and 250 μm , respectively. Heeschen et al. [41] showed an improvement in hydrate formation induction time for small particle sizes and claimed that this could be related to: (1) the increase in surface area and pore space with decreasing particle size, which enhances gas and liquid contact and promotes nucleation and hydrate growth. (2) mineralogical and/or morphology changes associated with the decrease in particle size causing chemical and physical alterations in grain surfaces, which positively affect hydrate nucleation. Ge et al. [40] investigated the influence of the effect of particle size on methane hydrate formation and dissociation in silica sand. Two particle size ranges (0.18–0.25 and 0.3–0.9 mm) were considered. The authors found that water to hydrate conversion increases with decreasing particle size, and hypothesized that the surface area and pore space increase with decreasing particle size, which enhances the gas and liquid contact. Furthermore, when investigating the dissociation rate at different particle sizes, the dissociation rate is found to be lower with a larger particle size. The authors deduced from their experiments that decreasing particle size can enhance the amount of hydrates formed in the pore space.

The water saturation of the porous media controls the quantity of hydrate that will potentially be formed. Several studies have investigated the link between water saturation and the amount of hydrate formed in silica sand, and the results vary widely from one study to another: Using magnetic resonance imaging, Bagherzadeh et al. [43] observed an optimum water conversion to hydrate at 75% water saturation. Hydrate growth formation is observed to be occurring faster at low water saturation. Indeed, at low water saturation, the likelihood of hydrate plugs forming is reduced, allowing methane

to diffuse easier through pore space. The experiments also demonstrated that methane hydrate nucleation in silica sand is spatially inhomogeneous, giving rise to the formation of several hydrate nucleation loci at different times along the bed of silica sand. Kumar et al. [44] report a maximum water conversion to hydrate of 60% at 75% water saturation in silica sand. Ge et al. [40], also studied the effect of water saturation on methane hydrate formation and dissociation in silica sand. Three water saturations (50%, 70% and 90%) were tested at 277.15 K and 8 MPa. According to Ge et al. [40] water conversion to hydrate reach an optimum at 70% water saturation, and the gas uptake obtained at 90% water saturation is considerably lower (up to > twice lower) than that obtained at 50% and 70% water saturation. The significant difference in water conversion and gas uptake is due to the non-uniform water distribution in silica sand at 70% than at 90% saturation.

Experimental studies on the link between the methane injection flowrate and the hydrate formation kinetics in sand are even scarcer. Ruffine [45] showed that induction time decreases with increasing methane flowrate for experiments at 40% water saturation.

This study investigated the effects of sand particle sizes, initial water saturation and methane injection flowrate on hydrate formation kinetics and gas storage capacity. It contributes to a continuing laboratory effort to better understand hydrate dynamics and properties.

2. Materials and Methods

2.1. Materials

The methane used in the experiments (claimed purity of 99.99%) was supplied by Air Liquide (Saint-Priest, France). Fontainebleau silica sand (Laboratoires Humeau, La Chapelle-sur-Erdre, France) was used as the porous medium. Figure 1 shows the particle size distribution of the calibrated sand.

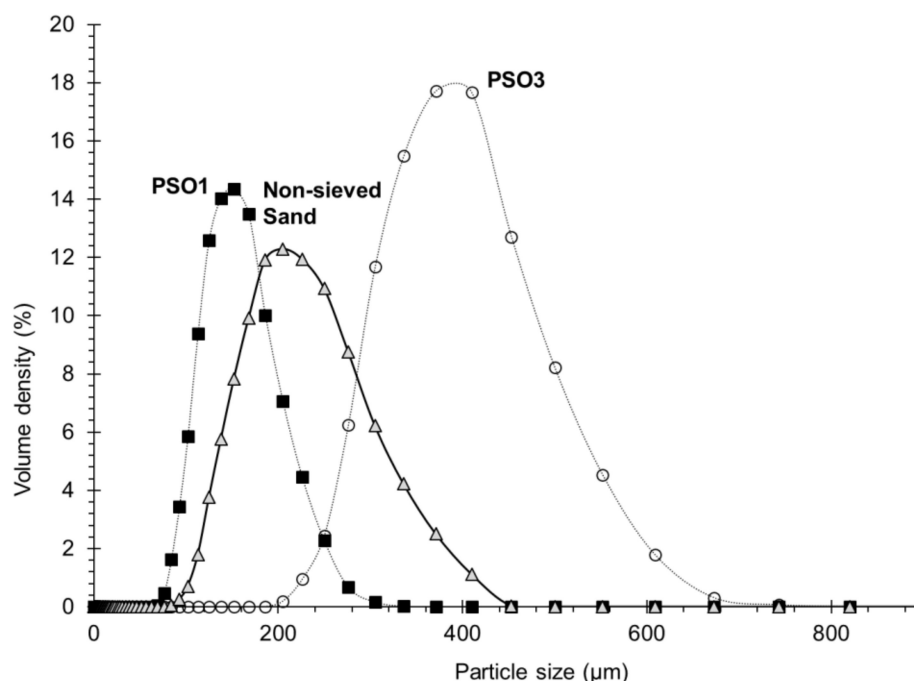


Figure 1. Experimental particle size distribution of calibrated Fontainebleau sand by diffractometer analysis: (Δ) non-sieved sand; (\blacksquare) class PS01 particle; (\bullet) class PS03 particle. Lines are used only to guide the eye.

The grain size ranged from 80 to 450 μm , with the dominant fraction size ranging between 140 and 315 μm . Deionized water was used after boiling to evacuate the residual dissolved gas. For the study of the effect of particle sizes, the sand was sieved and divided into two classes of particle size: PS01 ranging from 80 to 140 μm and PS03 from 315 to 450 μm . Table 1 shows the mass proportions of each

class per 100 g of Fontainebleau sand. A Mastersizer 3000 laser diffractometer (Malvern, Worcestershire, UK) was used to measure sand particle size distribution (PSD). The analysis of particle size of PS03 showed the presence of few individual particles or agglomerates larger than 450 μm and up to 550 μm , representing a very small mass proportion of the whole non-sieved sand batch, and therefore were neglected. For PS01 sieve, we noticed particles or agglomerates of sizes up to 200 μm . This study assume that this is due to the non-spherical shape of the particles, which are able to pass through the sieve mesh according to the particles' orientation angle.

Table 1. Mass proportions of different classes of Fontainebleau sand particle size.

Particle Class	Fontainebleau Sand	PS01	PS03
Particle size by sieving (μm)	80–450	80–140	315–450
Particle size by diffractometer analysis (μm)	80–450	80–200	200–550
Mass (g)	100	5.8	4.2

2.2. Experimental Setup

A schematic diagram of the experimental apparatus used for this study is shown in Figure 2. This apparatus has been described in a previous study by Ruffine [45].

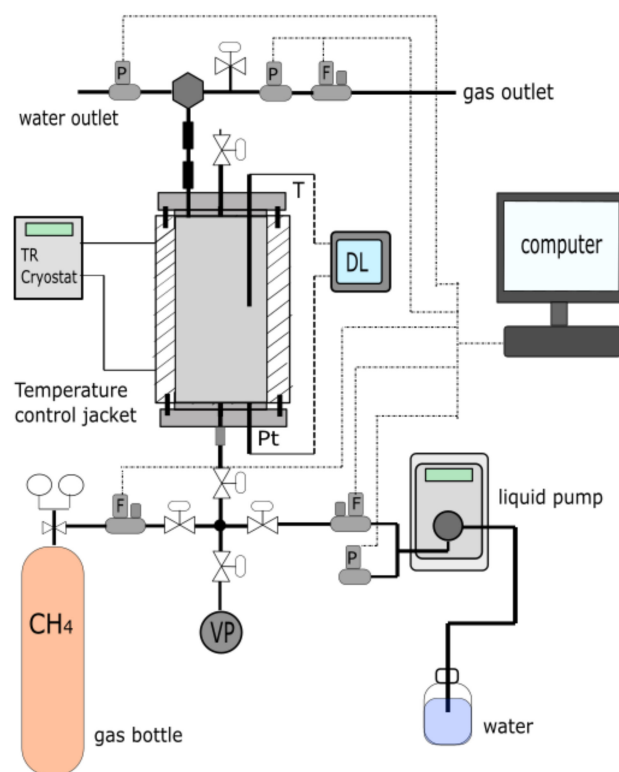


Figure 2. Schematic diagram of the experimental apparatus. (DL) Data logger, (P) Pressure regulator, (F) Mass flow regulator, (Pt) Pressure transducer, (T) Thermocouple, (TR) thermal regulator, (VP) Vacuum Pump, (⊙) high-pressure filter for gas-liquid separator, (⊖) high pressure 0.5 μm filter.

Briefly, it consists of a high-pressure cylindrical cell (HPC) with a functional volume of 508 mL. The apparatus was designed for hydrate-bearing sediment cores of around 170 mm long and 60 mm diameter, to withstand pressure up to 22 MPa for a temperature range of 253 K and 373 K. The temperature in the cell is controlled by circulating a coolant fluid containing water and ethanol (50/50%–vol) in a double jacket. The cell is connected upstream and downstream to a circuit equipped with HP manual valves, as well as fluid flow and pressure regulators for the injection of water and gases

at desired flowrate and controlling pressure within the cell. To facilitate homogeneous distribution of fluids in the porous media, two porous stones with a diameter of 54.6 ± 0.8 mm and 5.9 ± 0.2 mm-thick are placed at the top and bottom of the cell. Nevertheless, the water distribution remained relatively heterogeneous over the sediment core. Temperature is measured by means of a 150 mm-long K-thermocouple fixed on the upper flange of the cell with a measurement uncertainty of ± 0.2 °C. Both upstream and downstream pressures can be monitored using a type P-31 pressure transducer from Wika (Klingenberg, Germany) located on the lower flange of the cell and a pressure regulator located close to the thermocouple, respectively. The measurement uncertainty are of ± 0.02 MPa and 0.5 MPa, for respectively the pressure transducer and the pressure regulator. Both pressure and temperature were monitored over time with a data recording-resolution of 10 s.

2.3. Experimental Method

Methane hydrates were first formed as follows: The cell was filled with dried silica sand. The total amount of sand introduced was calculated by a weight difference method before and after filling the cell, with an uncertainty of ± 0.1 g. Later, the cell was evacuated using a vacuum pump, then filled with a desired amount of water at a flowrate of $2.5 \text{ g}\cdot\text{min}^{-1}$, and maintained at a temperature of 293.15 K for at least 15 h to ensure no ongoing water movement due to gravity before the gas injection. The amount of water expressed in mL corresponding to the desired water saturation, S_w , was calculated as follows:

$$V_v = V_{\text{cell}} - 2 \times V_{\text{ps}} - V_s, \quad (1)$$

$$V_w = S_w \times V_v, \quad (2)$$

where, V_v (mL) represents the volume of the void space, V_{cell} (mL) is the cell volume, V_{ps} (mL) is the volume of the porous stone and V_s (mL) is the volume of the sand calculated from the sand density (see Table 2).

Table 2. Aluminum cell and porous stone parameter.

Porous stone diameter (cm)	5.54 ± 0.88
Aluminum cell internal diameter (cm)	5.6 ± 0.01
Aluminum lids internal diameter (cm)	0.57 ± 0.01
Porous stone depth (cm)	0.6 ± 0.2
Aluminum cell height (cm)	13.94 ± 0.01
Aluminum lids height (cm)	5.55 ± 0.01
Sand density ($\text{g}\cdot\text{cm}^{-3}$)	2.65 ± 0.01
Porosity	0.42 ± 7.10^3

Afterwards, the cell temperature was set to 276.15 K. Once the thermal stability was reached, methane was injected at the desired flowrate until a pressure of ~ 10 MPa was reached. The final pressure was held for at least 15 h to check for further hydrate formation and methane consumption. The incipient of hydrate formation during gas injection was characterized by a sudden pressure drop and an increase in temperature as shown in Figure 3a.

The second step corresponds to hydrate dissociation by depressurization. A pressure of 1 MPa was set to the downstream pressure regulator which is coupled with a gas flow meter. This system releases methane at a constant rate of $3.5 \text{ mL}\cdot\text{min}^{-1}$ until reaching the set pressure. The cell was then unsealed, cleaned and prepared for the next experiment.

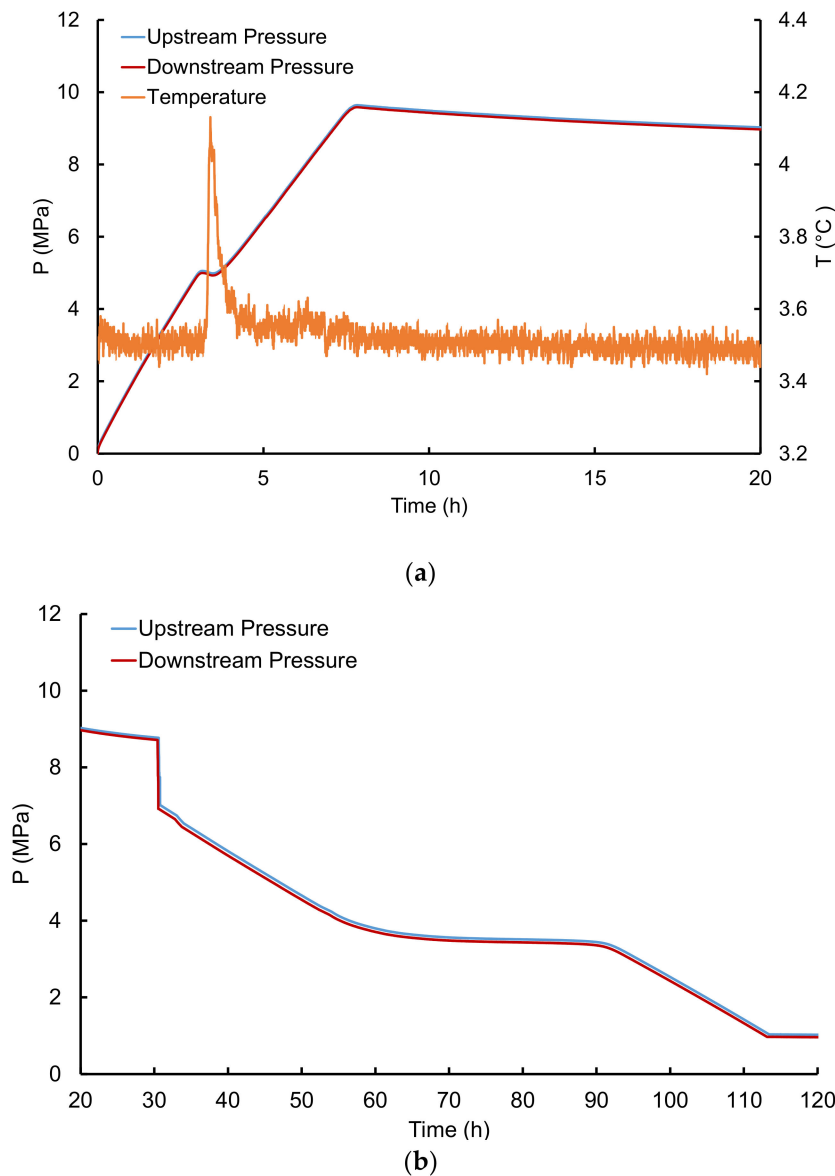


Figure 3. Evolution of upstream and downstream pressures with time. During (a) the formation and (b) depressurization step. The pressure in the cell decreases gradually during depressurization due to the release of free methane. The sudden drop observed in (b) at around 30 h is likely due to the breaking or dissociation of a hydrate plug that, at some point during the hydrate formation step, isolated a volume of the core from the remaining and hindering the gas to further accumulate. Thus, their reconnection after the dissociation of the plug leads to a pressure drop and equilibration. When the system reaches the H-L-V equilibrium pressure, hydrates begin to dissociate and release the methane previously stored. The pressure in the cell remains practically constant during hydrate dissociation. The procedure used for the quantification of hydrate-bound methane was developed by Ruffine in a previous work. The difference between hydrate formation pressure and hydrate dissociation pressure is detailed in Section 3.2.1.

The amount of gas released by the hydrates $V_{\text{gas_hyd}}$ is estimated as follows:

$$V_{\text{gas_hyd}} = Q_v \times \Delta t, \quad (3)$$

In this equation, Q_v corresponds to the depressurization gas flowrate (set at $3.5 \text{ mL}\cdot\text{min}^{-1}$), and Δt is the elapsed time for which the hydrates dissociate (plateau in Figure 3b). The amount of

water converted into hydrates during the pressurization step m_{wc} , was calculated from the gas volume released by hydrates in normal conditions (mLn) following Equation (4). Water conversion is then deducted using Equation (5):

$$m_{wc} = (V_{gas_hyd} \times M_w \times n_h) / V_m, \quad (4)$$

$$C_w = m_{wc} / m_{wi} \quad (5)$$

where V_m , expressed in $mL \cdot mol^{-1}$, is the molar volume of the gas in normal conditions and n_h is the hydration number. For methane hydrate structure sI with a single occupation cage, the hydration number is commonly taken as 5.75 [46,47] under our experimental conditions. m_{wi} is the initial mass of water introduced into the system.

2.4. Study of Water Distribution by X-Ray Computerized Tomography (CT Scan)

This study conducted X-ray computed tomography (CT) imaging experiments on a Geotek MSCL-XCT (Geotek Ltd., Daventry, UK) to have a clear appreciation of the water distribution in sandy cores. The maximum beam energy was around 130 kV. The scanning voltage and electricity were around 125 kV and 289 μA , respectively. The sample was rotated with a steep angle of 0.4° over 360° and data were collected as TIFF images with a typical image resolution of 960×768 pixels (better than $50 \mu m$). Orthogonal and circumferential images were processed using Geotek software to perform visual analysis of the core slices.

Several tests were performed on sandy cores at varying water saturation rates. To facilitate core recovery, the sand was introduced into an aluminum cell (Figure 4) that fits inside the HPC cell. The aluminum cell dimensional parameters are presented in Table 2. Both the lid and the bottom of the aluminum cell were drilled with 1 mm diameter holes over their entire surface to facilitate fluid flow, and the two porous stones were placed at the top and the bottom, respectively. For the sample preparation, the same procedure described in Section 2.3 was followed. Keep in mind that now the sand and water were introduced inside the aluminum cell. After water injection, the system was left for at least 18 h at ambient temperature, and then the aluminum cell was removed from the HPC cell and immersed immediately in liquid nitrogen for at least 3 h to freeze the water. This step ensures that there is no additional water movement in the void volume prior to analysis on the CT scanner.

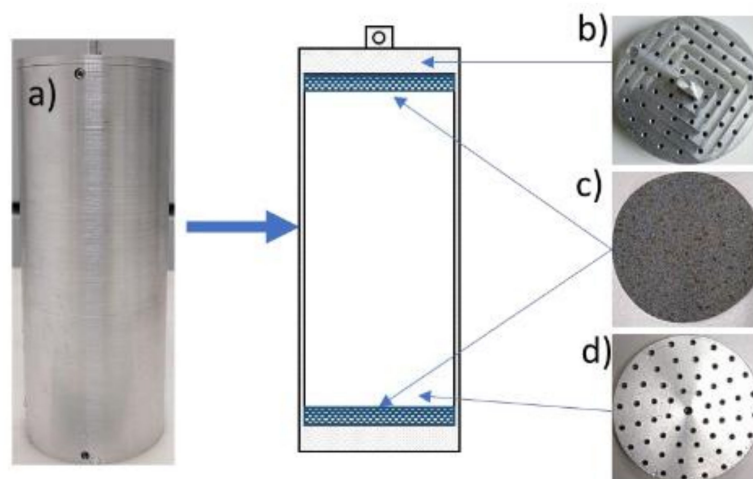


Figure 4. Photos and description of the interior of the aluminum cell: (a) aluminum body, (c) porous bauxite stones, (b,d) perforated aluminum lids.

3. Results

3.1. Water Distribution in Sandy Core Samples

The study of the water distribution pattern in the porous media prior to methane injection provides information on the extent of the wet volume within the core. This is essential to evaluate methane invasion within the remaining empty pore spaces and to witness how water spreads through the pore space. Four experiments followed by CT scanning tests were performed for this purpose at water saturations of 10%, 30%, 50% and 75% of the void volume. Figure 5 presents the reconstructed images from the water distribution tests. In each image, one can clearly identify the different components of the analyzed core-bearing aluminum cell: A: The upper perforated lid of the aluminum cell. B: The porous stone at the top in the black rectangle. C: The dry or wet sand. D: The wet front spreading down to the sandy column. E: The wall of the aluminum cell. F: The porous stone at the bottom. G: The bottom perforated lid. H: The space occupied by the type K thermocouple before freezing the core in liquid nitrogen (visible for the experiments at 10% and 30% water saturation). I: The water concentration zone. J: A network of cracks affecting the volume of sand in most tests. These cracks only occur in wet sand since they result from a frost shattering process that randomly fragments the water-saturated sand following its freezing in liquid nitrogen.

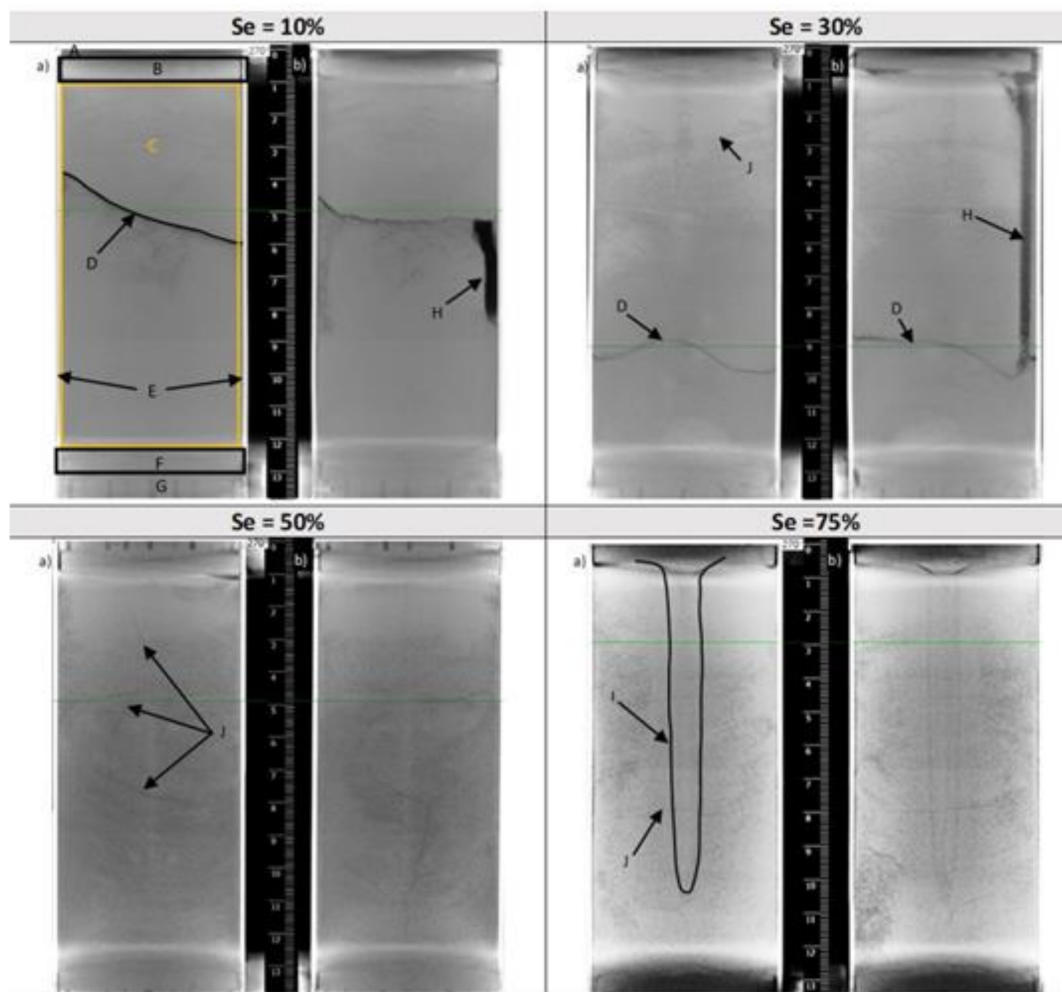


Figure 5. Orthogonal views of tomographic images of the sandy core for different water saturations (1) 10%, (2) 30%, (3) 50%, (4) 75%: (a) and (b) are orthogonal orientations. (A, E, G) Aluminum walls, (B, F) porous bauxite stones, (D) waterfront, (H) Thermometer hole, (I) high-water-content region, (J) cryogenic fracturing.

CT scan images of water distribution experiments and visual analyses show that:

- (1) Water injected at the top of the cell is heterogeneously distributed in the sandy core by capillary forces for 10% and 30% water saturation, in agreement with a previous finding [48]. Moreover, the amount of injected water is not sufficient to reach the bottom of the cell and a non-planar water front separating the wet and dry core sections is observed in Figure 5D. When the water saturation increases from 10% to 30%, this water front moves towards the bottom of the cell. The penetration depth of the water is between 4 cm and 6 cm thickness at 10% saturation, and between 8 cm and 10 cm thickness at 30%.
- (2) For higher water saturations (50% and 75%), the interface between the wet and dry core sections is not observed: it can be assumed that the amount of water is sufficient to reach the bottom of the cell. This is supported by the fact that the network cracks (J) reach the bottom of the cell at 50% water saturation. However, these CT scan images do not provide detailed and conclusive information on the total wettability of the core, and some zones remain dry suggesting a spatial heterogeneity as observed by Song et al. [49]. Therefore, Figure 5 should not be taken as face value but rather as an illustration of how heterogeneities linked to the intrinsic properties of the sandy particles (porosity and permeability) can be reflected in the water distribution. The computed porosity of the sandy core is around 0.42 here. Intrinsic permeability measurements were not carried out as our apparatus was not designed for this purpose. However, it was possible to calculate a first-order estimate of the hydraulic conductivity (k) using two widely used formula for coarse-grained matrices: The correlation from Hazen (1892) that correlated k with the effective diameter of the finest 10% of the sand (D_{10}), and an analytically derived Kozeny-Carman's equation from Ren et al. (2018) which is a function of the specific surface area of the sand [50–54]. The hydraulic conductivity is proportional to the intrinsic permeability, and gives an idea on how water flows through the sandy core. Here, computed hydraulic conductivity values are of (in $\text{cm}\cdot\text{s}^{-1}$) from 2×10^{-2} to 5×10^{-2} , from 1×10^{-2} to 3×10^{-2} and from 6×10^{-2} to 17×10^{-2} for the non-sieved sand, and the fraction PS01 and PS03, respectively. The highest values are obtained with the correlation derived from Kozeny-Carman's equation. As expected, the hydraulic conductivity increases with increasing particle size. These values are in agreement with values from the literature for sand with similar D_{10} [51–53]. Overall, there is less than one order of magnitude between the hydraulic conductivity of each sand fraction. Knowing the non-compressibility of sand particles, we can reasonably consider here a narrow distribution range for their intrinsic permeability of the core and a diversity in the flow paths due to differences in size and shape of the particles, thus, explaining the heterogeneity in the porosity and permeability fields. In fact, the non-planar water front after water stabilization at 10 and 30% water saturation results from heterogeneity in the porosity and permeability fields. Thus, it is likely that even if the same procedure for sample preparation is repeated with the same matrix and at the same water saturation, the water distribution may differ from one experiment to another. At 75% water saturation, we noticed the presence of a region with a cone-like shape located in the center of the core. This region corresponds to a water saturated zone as the water injection point is located at the center of the cell lid, this assumption was confirmed when emptying the cell to visually examine the sandy core. The small region with a cone-like shape of wet sand was indeed visible, and it took longer to defrost compared to the rest of the matrix.

3.2. Hydrate Formation: Variability of the Induction Time and Pressure Induced Growth Trajectory with the Three Selected Parameters

This section focuses on the influence of water saturation, particle size and methane injection flowrate on the induction time. We also discuss how hydrates accumulate within the HPC cell through the description of the pressure profiles that sometimes highlight a loss in hydraulic connectivity (e.g., formation or not of hydrate plugs hindering the gas flow throughout the core).

3.2.1. Evolution of Induction Time for Repeated Experiments

Five methane hydrate formation and dissociation experiments were performed under the same operating conditions to investigate how the induction time evolves using non-sieved sand, at 53–57% water saturation and a gas flowrate of $\sim 58 \text{ mLn}\cdot\text{min}^{-1}$. The results obtained are summarized in Table 3 (see highlighted data, also identified as experiments from 5_1 to 5_5). It can be noticed that the pressure for the incipient of hydrate formation is different from and higher than the pressure of dissociation. Hydrate formation is controlled rather by kinetics than thermodynamic equilibrium. Therefore, hydrate formation starts at pressure beyond the equilibrium pressure (for experiment temperature here, the equilibrium pressure is ca. 3.5 MPa). These two pressures, the equilibrium pressure and the formation pressure, allow determining the induction time. Indeed, the induction time is defined as being the elapsed time starting from when the increasing pressure of the system reaches the thermodynamic equilibrium pressure to the detection of the first pressure drop indicating hydrate formation. The change in the slope of the pressure vs. time curve is often combined with a peak in temperature due to the exothermic nature of hydrate formation. The intensity of this peak in temperature strongly depends on the proximity of the hydrate growth loci within the sandy core to the thermocouple.

Table 3. Key measured parameters related to methane hydrate formation and dissociation experiments with varied water saturation conditions.

Run.	Water Volume (mL)	Water Saturation, S_w (%)	Gas Flowrate (mLn/min)	Particle Size (μm)	Induction Time (min)	Volume of Hydrate-Bound Methane (Ln)	Water Conversion (% vol)
1	23.34	10.8	56.1		53	4.94	97.8
2	46.6	21.6	58.5		65	8.27	82.0
3	72.4	33	58.4		148	10.50	67.0
4	92.69	44	57.6		63	15.82	78.9
5_1 *	116.5	53	57.5	80–450	82	15.48	61.4
5_2 *	116.1	54	58.8		57	12.44	49.5
5_3 *	117.3	54	57.2		55	14.77	58.2
5_4 *	117.8	55	57.9		51	20.94	82.1
5_5 *	124.8	57	57.5		47	20.43	75.6
6	144.9	66.3	58.2		69	25.43	82.7

* The highlighted corresponds to experiments performed at constant operating conditions.

The evolution of pressure during the hydrate formation step for the five aforementioned experiments is also shown in Figure 6. For all experiments, the pressure increases linearly with the methane injection until the occurrence of a sudden pressure drop due to hydrate formation by the gas uptake. Thereafter, pressure starts to increase again with smaller fluctuations until reaching injection pressure. Similar behavior in pressure drops and fluctuations was observed by Song et al. [49] for hydrate formation in fully water-saturated glass beads under constant methane flowrate. The induction time determined for the five experiments are summarized in Table 3. The values are relatively scattered, with an average value of 58 ± 14 min. However, if we decide to remove experiment 5_1, and consider only the last four of the five experiments (5_2, 5_3, 5_4, and 5_5), the values of induction time become more homogeneous, with an average value of 53 ± 5 min; highlighting values closer to each other. Accordingly, only experiment 5_1 exhibits a significantly different induction time from the others. Knowing that the very same procedure was applied for all experiments, the reason for which experiment 5_1 gave rise to a delay in induction time remains quite elusive, but it certainly expresses the stochastic nature of hydrate nucleation step as discussed in previous studies [45,55–57]. Alternatively, the occurrence of tortuosity, differences in particle size and pore-throat shape lead to heterogeneity in the porosity and permeability fields of the sandy core that affects the contact surface between the water and methane, and consequently influences the hydrate formation kinetics [58,59]. Such a heterogeneity can also explained the time delay here.

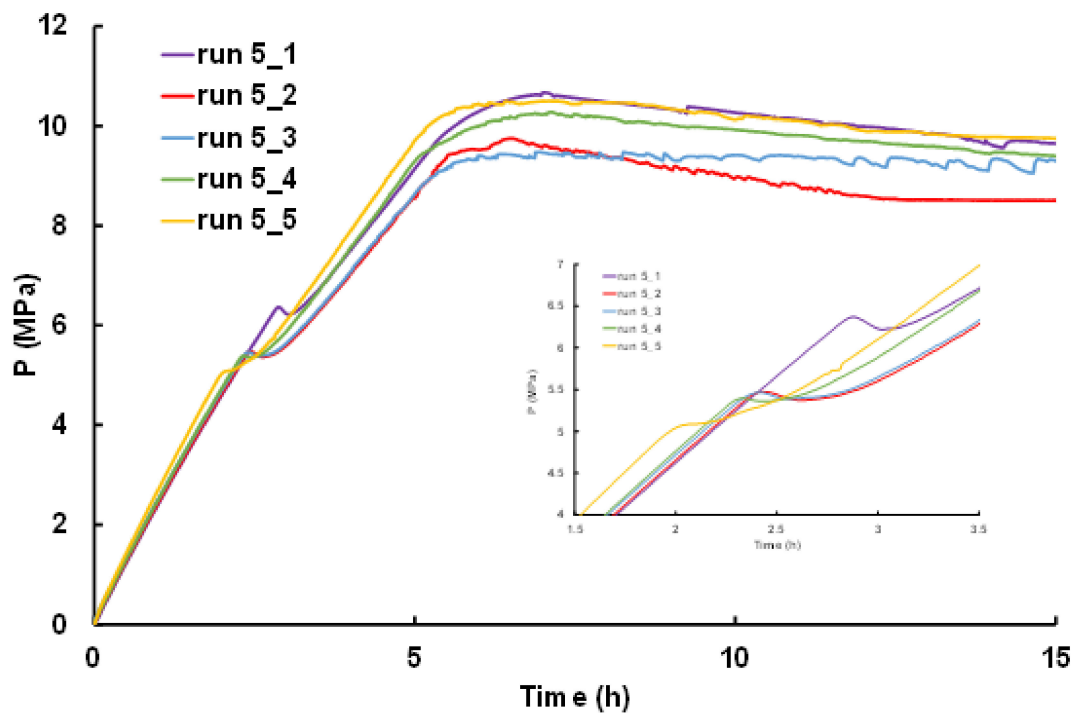


Figure 6. Pressure-time profile during hydrate formation experiments at constant operating conditions.

Interestingly, the induction times determined here are shorter than those obtained by Ruffine [45] from six repeated experiments at the same methane injection flowrate and 40% water saturation. He found an average value of induction time of 89 ± 33 min. Thus, this comparison suggests that the induction time globally decreases with increasing initial water saturation, but this needs to be confirmed by additional series of repeated experiments at a third water saturation.

3.2.2. Influence of Water Saturation

Figure 7 shows the upstream and downstream pressure and temperature evolution as a function of time for gas hydrate formation and dissociation experiments at a water saturation rate varying from 10.8% to 66.3% (the gas flowrate and particle size remain constant). For water saturation lower than or equal to 33%, the two curves of upstream and downstream pressure match perfectly (in Figure 7a–c), indicating a permanent hydraulic connectivity over the course of the experiments. For higher water saturation (Figure 7d–f), the upstream and downstream pressures show different trajectories over time, indicating differences in pressure at the two core ends probably caused by the formation of hydrate plugs in the pore space and/or at the inlet and outlet of the cell. It is obvious that the probability of creating plugs increases with increasing water saturation. However, it is worth noticing that the level of water saturation at which the loss in hydraulic connectivity is observed (>33%) coincides more or less with the water saturation values from which the water migrates close to the bottom of the sandy core as was observed from the CT-Scan analysis (Figure 5).

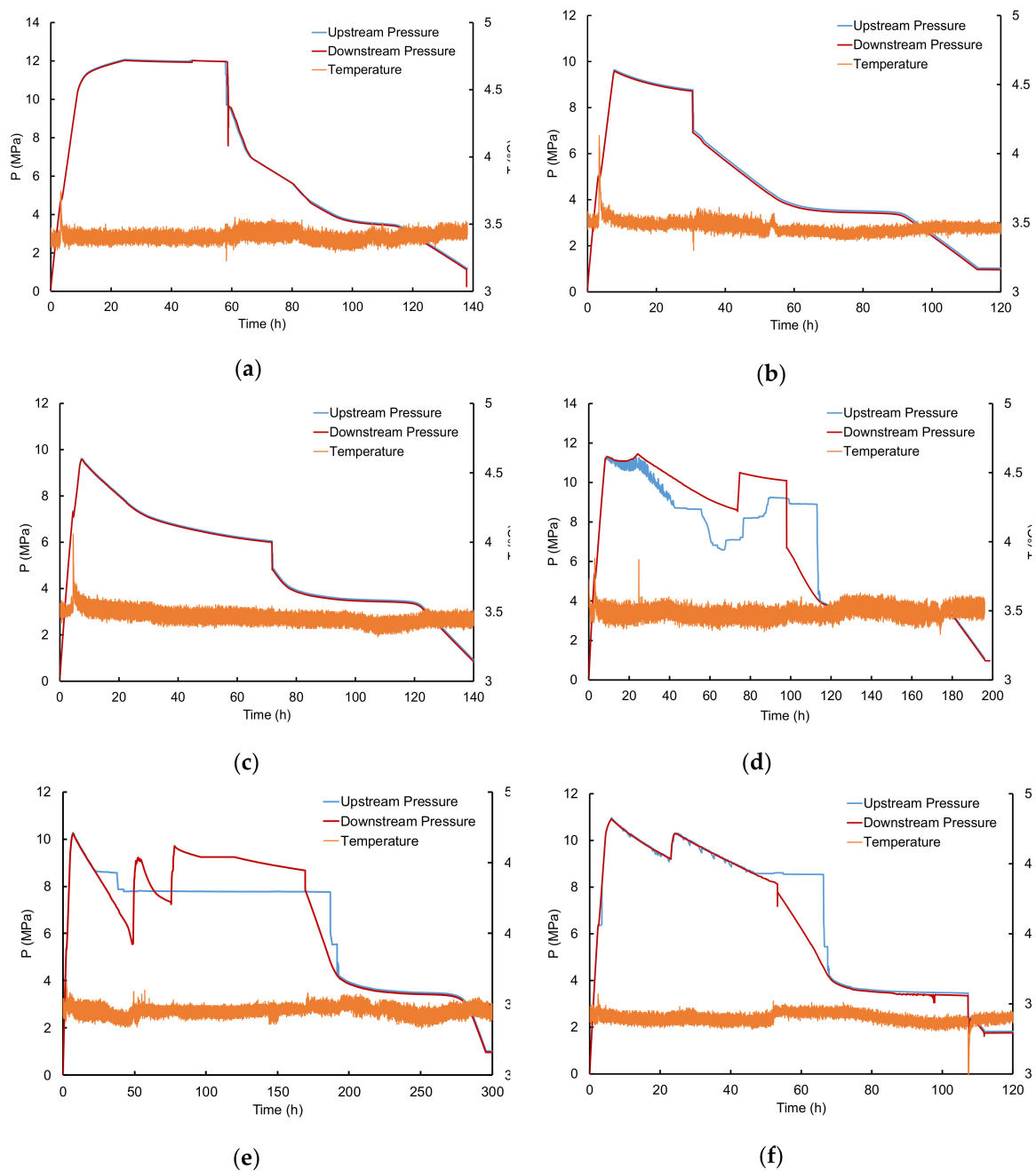
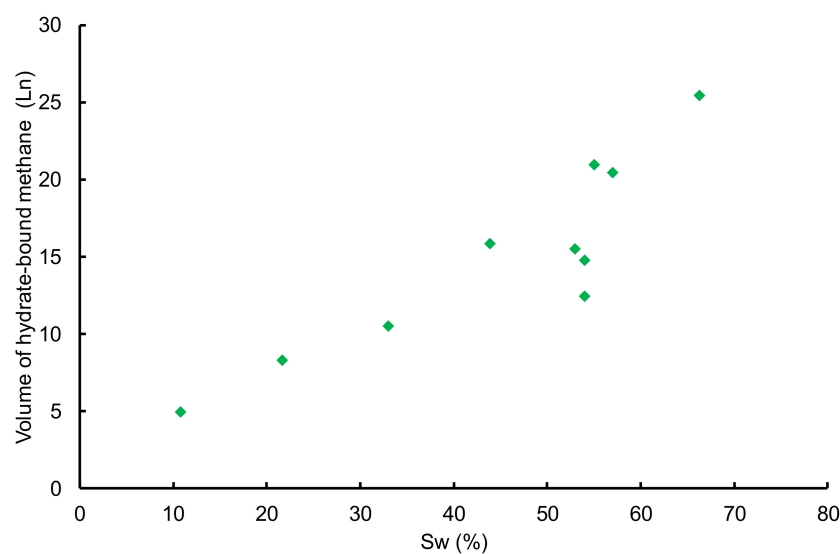


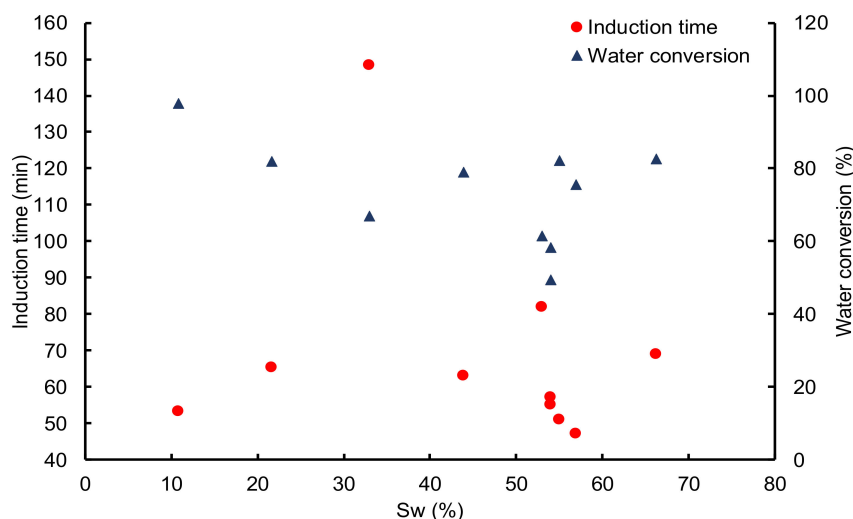
Figure 7. Upstream and downstream pressure and temperature profiles for experiments with non-sieved sand, a gas flowrate around $58 \text{ mLn}\cdot\text{min}^{-1}$ and different water saturations S_w : (a) $S_w = 10.8\%$; (b) $S_w = 21.6\%$; (c) $S_w = 33\%$; (d) $S_w = 44\%$; (e) $S_w = 55\%$; (f) $S_w = 66.3\%$.

During the hydrate formation step, methane is continuously injected into the high-pressure cell until the system pressure reaches the cylinder pressure ($\sim 10.5\text{--}11 \text{ MPa}$), and then, the injection is stopped. However, during this period of no-methane injection, the hydrate formation continues within the cell, with methane gas consumption and a decrease of the cell pressure. Consequently, the pressure balance between the gas cylinder and the high-pressure cell is breaking, the methane injection resumes and the cell pressure increases again. This switch between balance and unbalance between the cylinder and the cell pressure explains the up and down oscillations observed between 10–25 h on the upstream pressure in Figure 7d–f. Thereafter, the gas injection is definitely stopped by closing the inlet valve of the cell.

Figure 8b and Table 3 show significant scattering in the induction time determined from experiments performed at different water saturations, with values ranging between 47 and 148 min. Such results do not highlight any clear link between water saturation and the induction time. They are in line with previous conclusions [55], but not consistent with Wang et al. [60] where a clear relationship is found between the induction time and water saturation for hydrate formation in glass beads; with an optimum time achieved at 70% water saturation. However, the porous medium used and the experimental procedure applied were different. The induction time has an average value of 69 ± 30 min. However, this averaged induction time decreased to 58 ± 8 min if we do not consider run 3 and run 5_1 for which the induction times are 148 min and 82 min, respectively. Coincidentally, our first two series of experiments performed at a constant methane injection flowrate, lead to the conclusion that most of the experiments (80%) are characterized by an induction time close to each other; and the obtained value is alleviated by 10–15% of the averaged induction time over all the experiments defining these series.



(a)



(b)

Figure 8. (a) Volume of hydrate-bound methane as a function of water saturation; (b) Induction time and water conversion as a function of water saturation. The experiments were carried out with a non-sieved sand sample and a gas flowrate around $58 \text{ mLn}\cdot\text{min}^{-1}$.

3.2.3. Influence of Particle Size

As mentioned above, we also conducted several experiments at different particle sizes to better understand the impact of this parameter on the formation and dissociation of methane hydrates in a sandy core (Table 4). Three different classes of particle size (PS01, non-sieved sand, PS03) were compared for water saturation ranging between ~51 and 55%.

Table 4. Operating conditions and results obtained for methane hydrate formation and dissociation experiments with different classes of particle size and different gas flowrates.

Gas Flowrate (mLn·min ⁻¹)	Water Volume (mL)	Water Saturation, S _w (%)	Particle Size Class (μm)	Induction Time (min)	Volume of Hydrate-Bound Methane (Ln)	Water Conversion (%)
56.8	129.0	54.3	PS01	83	23.91	86.0
57.9	117.8	55.0	non-sieved sand	51	20.94	82.1
58.0	117.2	54.6	PS03	52	21.83	86.1
28.9	125.9	53.7	PS01	129.5	22.74	83.5
29.0	115.7	54.2	non-sieved sand	85	21.59	84.0
28.8	111.3	50.9	PS03	109	17.81	74.0
86.5	125.7	53.3	PS01	40.3	17.05	62.7
87.6	115.9	53.9	PS03	30.3	21.29	84.9

Figure 9 illustrates the evolution of induction time as a function of particle size for three different gas flowrates. By focusing on the particle size, we cannot define a clear link between this parameter and induction time. However, even with a reduced number of experiments at a flowrate of 87 mL·min⁻¹, the data points in Figure 9 suggest the occurrence of a class of particle size for which the induction time is a minimum as proposed by previous work [37,40,41].

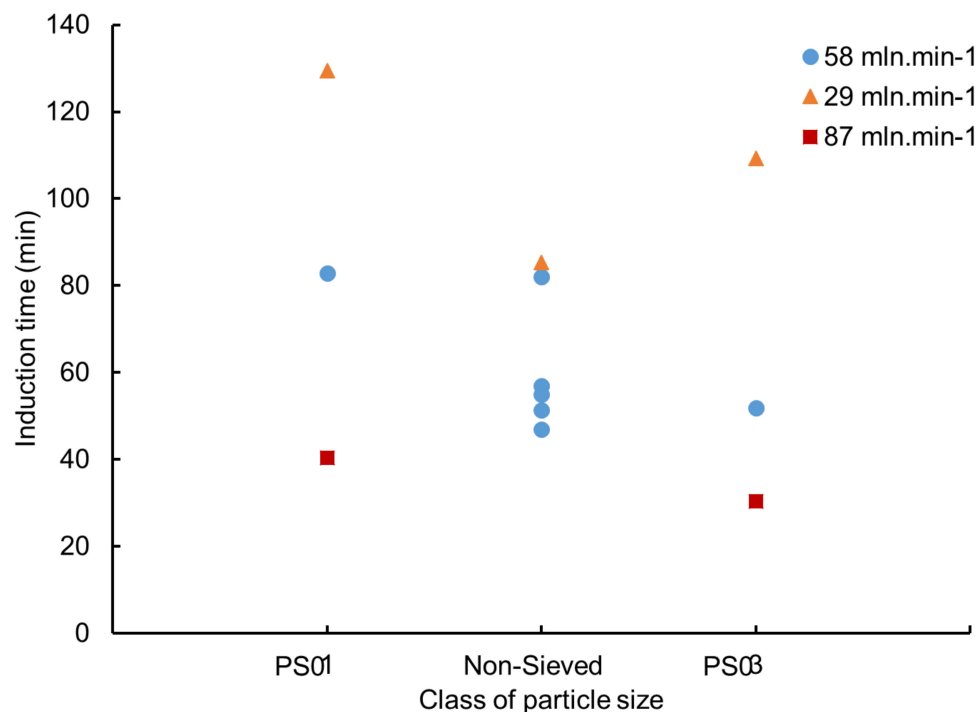


Figure 9. Induction time as a function of particle size for a water saturation around 53%.

Figure 10 illustrates the evolution of pressure and temperature during the first twenty hours of methane gas injection for the three particle size classes, at 53% water saturation and a methane injection flowrate of 29 mL·min⁻¹. For the experiment with the smallest particle size (PS01), we notice that

the pressure drop during hydrate formation is more pronounced and takes longer. Overall, pressure decreases when particle size increases. We also notice a duplication of the temperature peak and a larger drop in pressure in the case of PS01. This result is also observed in Figure S1, where the experiments were performed with methane injection flowrates of $50 \text{ mLn}\cdot\text{min}^{-1}$ and $87 \text{ mLn}\cdot\text{min}^{-1}$. The pressure drop illustrates the kinetics of the gas uptake (e.g., the kinetics of hydrate growth within the sandy core). The more pronounced the pressure drop, the faster the hydrate growth. In our case, we hypothesized that the smallest particles increase the available specific surface, offering a greater area for water distribution and enhancing the interfacial contact between water and methane. Such a configuration fosters the multiplication of hydrate nucleation sites and gives rise to several simultaneous or successive hydrate growth locations. This is in agreement with Ge et al. [40]. Indeed, the authors observed a decrease in gas uptake with increasing particle size of silica sand. The two temperature peaks observed in Figure 10 during the experiment using PS01 sand may also support the hypothesis that hydrate nucleation may occur on several locations along the sample core. Alternatively, the occurrence of two temperature peaks may also indicate alternating episodes in hydrate growth, with a short quiescent period in between.

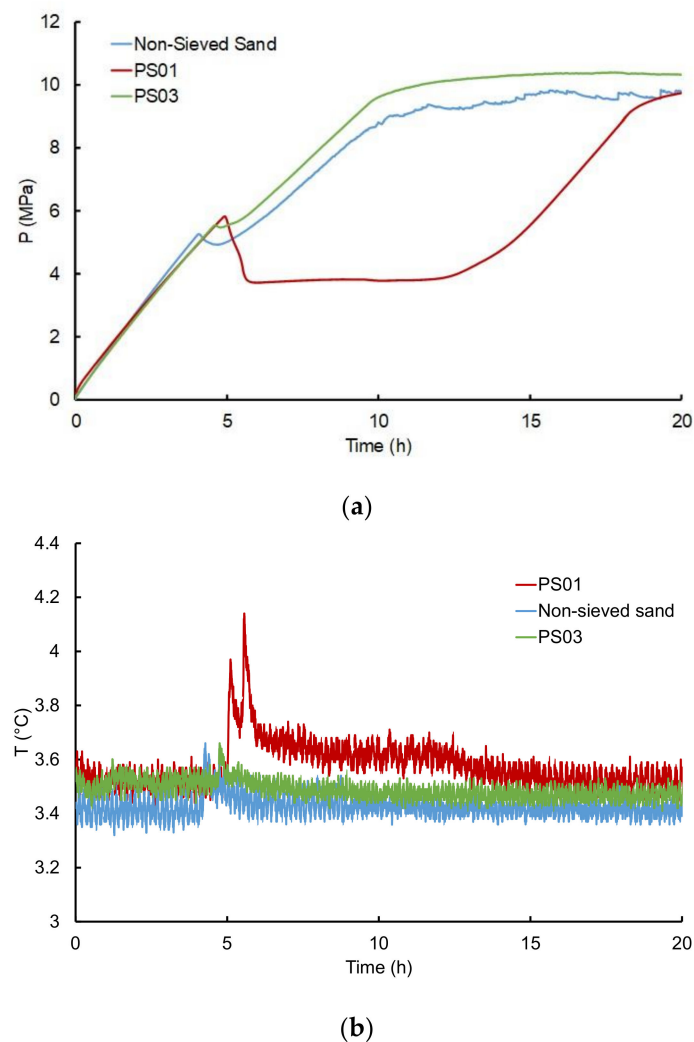


Figure 10. (a) Pressure and (b) temperature profiles during the methane hydrate formation step at around 53% water saturation and a gas flowrate of $29 \text{ mLn}\cdot\text{min}^{-1}$ with different classes of particle sizes.

3.2.4. Influence of the Gas Flowrate

Figure 11 illustrates the variation in induction time as a function of the gas flowrate for a water saturation of 50–57%. It shows undoubtedly that the methane injection flowrate has a significant influence on induction time, confirming a previous study performed at lower water saturation [45]. Overall, induction time decreases with the increase in the methane injection flowrate, and the time reduction is even larger for the smallest particle sizes. Indeed, for the smallest class of particle size PS01, an increase in the gas flowrate from 29 mL·min⁻¹ to 87 mL·min⁻¹ leads to a decrease of up to 90 min in the induction time. A similar evolution is observed for the class of particle size PS03. A high gas flowrate allows the system to achieve the favorable hydrate (p, T) conditions within the cell much faster, while saturating the void space with gas more rapidly. This result is in agreement with a previous study using the same apparatus at a water saturation of 40% and with particle sizes of 180–500 μm [45]. Interestingly, while the water saturation investigated in this study is at least 25% higher than the value in Ruffine's work [45], the induction times obtained are very similar.

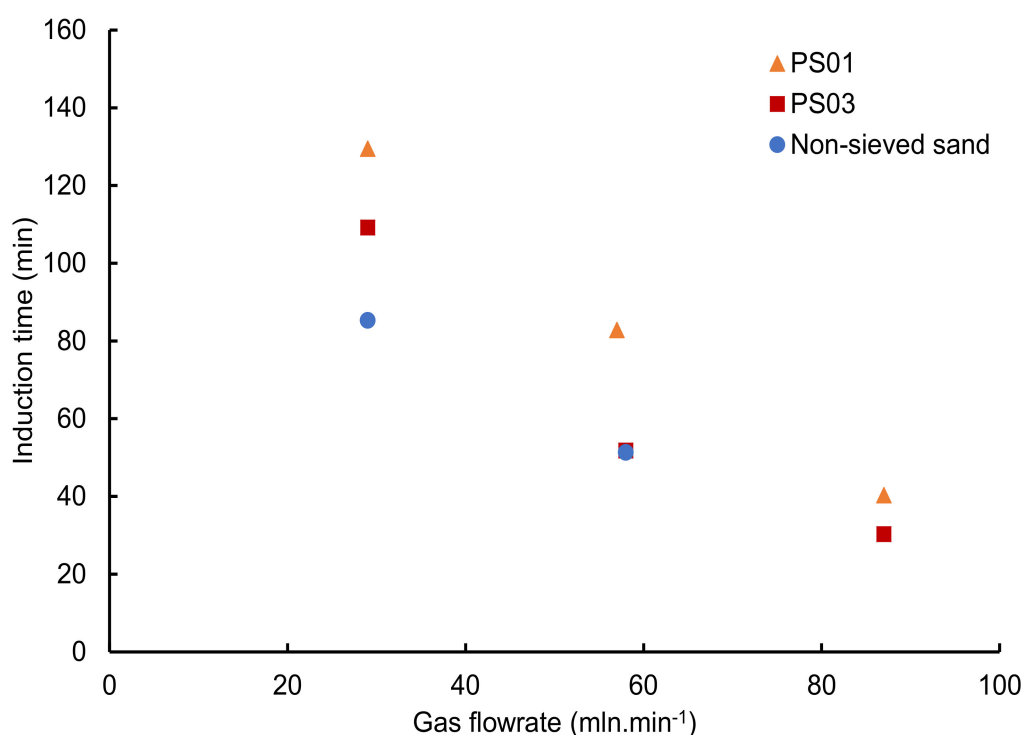


Figure 11. Induction time as a function of gas flowrate for a water saturation around 53%.

3.3. Influence of the Water Conversion, Gas Injection Flowrate and Particle Size on the Storage Capacity

The results presented in Tables 3 and 4 indicate that water conversion is never complete, with very heterogeneous values ranging between 49.5 and 97.8%. Nevertheless, a trend can be drawn from these results. Most of the estimates are around 80%. The highest water conversion is obtained at 10% water saturation because the amount of water is sufficiently low to be almost totally converted without the risk of forming hydrate plugs. The water conversion decreases with increasing water saturations up to 66.3% as observed by Ge et al. [40], and thereafter the conversion seems to reach an asymptote around 80% except for experiments 3, 5_1, 5_2, 5_3 (Table 3) where relatively low water conversions were obtained. In contrast, the experiments carried out by Song et al. [49] led to faster hydrate formation and higher hydrate saturation in fully water-saturated glass beads under constant methane flowrate. Therefore, it is likely that other factors, like the geometry and volume of the reactor, as well as the porosity and permeability fields affect water conversion.

Surprisingly from Table 4, irrespective of the flowrate and particle size, the mean value of water conversion ranges between 80–85%. Only the experiment using the PS01 class and a gas flowrate of $86.5 \text{ mLn}\cdot\text{min}^{-1}$ exhibits a clear deviation from this average with a water conversion of 62.7%, and the experiment using the PS03 class and $29 \text{ mLn}\cdot\text{min}^{-1}$ that shows 74% water conversion. Likewise, the volume of hydrate-bound methane increments with increasing water saturation as shown in Figure 8a. Our results are consistent with Ge et al. [40] who also observed an increase in the amount of hydrate-bound gases up to water saturation of 70%. However, while a clear link is observed between the volume of hydrate-bound methane and the water saturation, repeated experiments at a fixed water saturation show significant discrepancies in the estimated volume: the higher estimate is ~60% larger than the lower estimate. Therefore, the repeated experiments should be taken as an appreciation of the deviation from the trend, and recall for intensive series of experiments to fully capture the relationship between water saturation and the intrinsic porous-medium properties.

On the opposite, there is a lack of clearly visible link between the volume of hydrate-bound methane and particle size or gas flowrate (Figure 12). The volumes of hydrate-bound methane are scattered, and range between 17.05 Ln and 23.91 Ln. The lowest volumes of hydrate-bound methane obtained (i.e., 17.05 Ln and 17.81 Ln) corresponds to the lowest water conversion to hydrates (i.e., 62.7% and 74%). This is an expected result as these two parameters are linked via Equations (4) and (5). These low volumes of hydrate-bound methane can be explained by the formation of hydrate plugs that limits methane flow throughout the sandy core, and therefore limits the hydrate growth.

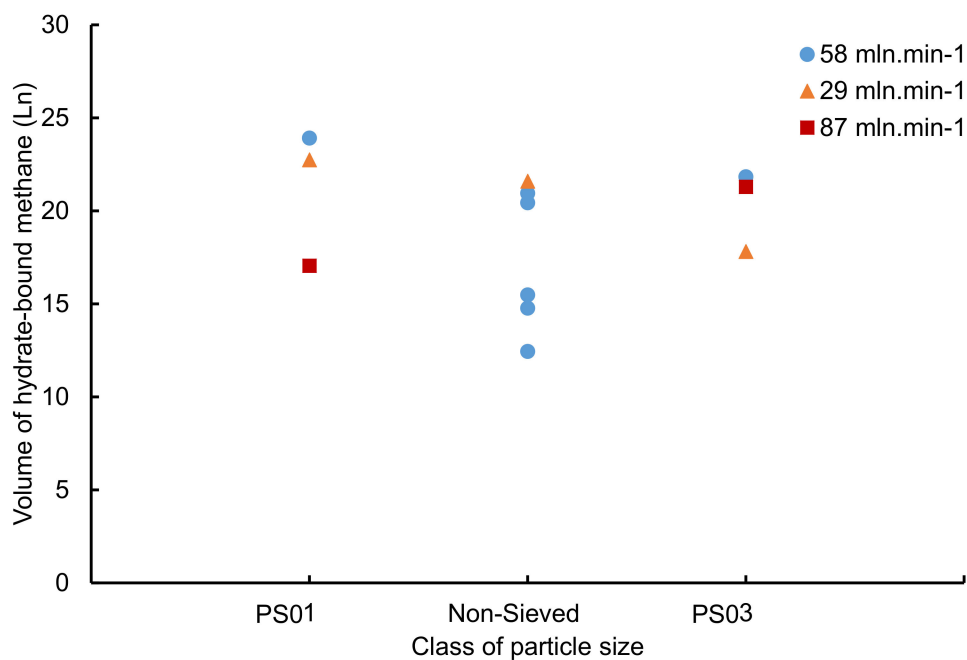


Figure 12. Volume of hydrate-bound methane as a function of particle size for a water saturation around 53% and different gas flowrates.

4. Conclusions

This study consists of a series of methane hydrate formation and dissociation experiments in a sandy core. Experiments were carried out in a synthetic sandy core to investigate the influence of water saturation, methane injection flowrate and particle size on: (1) induction time, and (2) hydrate storage capacity. A preliminary CT scan study showed how water is distributed within the core for different water saturations. The observed heterogeneous water distribution is likely linked to the heterogeneity in porosity and permeability fields due to the diversity of the particle size and shape. Overall, the water distribution is heterogeneous, irrespective of the water saturation level. The water

injected from the top never entirely reached the bottom of the sandy core, suggesting that the capillary effect is dominant over the gravity effect in at the investigated water saturations. The resulting CT scan images show that water is fully distributed from the top to the core bottom for water saturations of 50% and 75%, whereas a dry bottom section can be identified for lower water saturation. The whole set of experiments shows that the length of the wet zone increases with increasing water saturation.

The data showed that the three studied parameters significantly affect the hydrate-formation induction time. The methane injection flowrate shows the most unambiguous link with induction time. Increasing the injection flowrate clearly considerably decreases the induction time, irrespective of water saturation and particle size. This result is significant as it throws new light on the implication of fluid flow in the kinetics of hydrate formation in marine sediments. The independency of gas flowrate on the kinetics of hydrate formation with regard to water saturation and particle size provides a suitable key parameter of control for the development of industrial hydrate-based processes and technology. The influence of particle size and water saturation on induction time is less obvious as the results are more scattered. Our experiment has also revealed the existence of a threshold at 44% water saturation from which the formation of hydrate induces a loss in hydraulic connectivity, leading to differential pressure between the two ends of the sandy core. When water saturation increases, the volume of hydrate-bound methane increases. However, water is not totally consumed for most of experiments; water conversion values are around 80%. This incomplete consumption of water may be due to the formation of hydrate plugs which limits the contact between water and gas phases. Our results also show an independency between the volume of hydrate-bound methane and the water to hydrate conversion ratio. Overall, this work contributes to continuing laboratory efforts to better understand hydrate formation kinetics and its gas storage capacity.

Supplementary Materials: The following are available online at <http://www.mdpi.com/1996-1073/13/19/5200/s1>, Figure S1: Pressure and temperature profiles during the first hours of methane hydrate formation and dissociation experiments around 53 % water saturation, and a gas flowrate of (a) 87 mln.min⁻¹ with different particle sizes and (b) 50 mln.min⁻¹ for non-sieved sand.

Author Contributions: Conceptualization, F.D.B., L.R. and O.F.; methodology, F.D.B., L.R. and O.F.; validation, L.R., P.C., A.D., L.F., V.O. and O.F.; writing—original draft preparation, F.D.B.; writing—review and editing, F.D.B., L.R., O.F., P.C., A.D., L.F. and V.O.; supervision, L.R., P.C., A.D., L.F., V.O. and O.F. All authors have read and agreed to the published version of the manuscript.

Funding: This research received no external funding.

Acknowledgments: The authors would like to thank Laurène Bazinet, internship student from ENSG- Nancy at Ifremer, for her dedication in studying the water distribution on sandy core using X-ray tomography; and Mickael Rovere at Ifremer, for his advice and guidance with the CT-Scan. We are also grateful to Philippe Fernagu, Mickael Roudaut and Jean-Pierre Donval for their direct technical help and Marco Terzariol for useful discussions. We also thank Alison Chalm for the proofreading to the paper. The authors also acknowledge three anonymous reviewers for their valuable suggestions and remarks that greatly improved the manuscript. This study was undertaken in the frame of the French Research Consortium “GdR-2026 Hydrates de gaz”.

Conflicts of Interest: The authors declare no conflict of interest.

References

1. Sloan, E.D., Jr. Fundamental principles and applications of natural gas hydrates. *Nature* **2003**, *426*, 353–359. [[CrossRef](#)] [[PubMed](#)]
2. Loveday, J.S.; Nelmes, R.J. High-pressure gas hydrates. *Phys. Chem. Chem. Phys.* **2008**, *10*, 937–950. [[CrossRef](#)] [[PubMed](#)]
3. Broseta, D.; Ruffine, L.; Desmedt, A. *Gas Hydrates 1: Fundamentals, Characterization and Modeling*, 1st ed.; John Wiley & Sons: Hoboken, NJ, USA, 2017; p. 302.
4. Kvenvolden, K.A. Methane hydrate—A major reservoir of carbon in the shallow geosphere? *Chem. Geol.* **1988**, *71*, 41–51. [[CrossRef](#)]
5. Ruffine, L.; Broseta, D.; Desmedt, A. *Gas Hydrates 2: Geoscience Issues and Potential Industrial Applications*; John Wiley & Sons: Hoboken, NJ, USA, 2018.

6. Matveeva, T.; Mazurenko, L.L.; Soloviev, V.A.; Klerkx, J.; Kaulio, V.V.; Prasolov, E.M. Gas hydrate accumulation in the subsurface sediments of Lake Baikal (Eastern Siberia). *Geo Mar. Lett.* **2003**, *23*, 289–299. [[CrossRef](#)]
7. Ruppel, C.D. *Gas Hydrate in Nature*; US Geological Survey: Reston, VA, USA, 2018.
8. Dillon, W.P.; Max, M.D. Oceanic Gas Hydrate. In *Natural Gas Hydrate in Oceanic and Permafrost Environments*; Max, M.D., Ed.; Springer: Berlin/Heidelberg, Germany, 2003; pp. 61–76.
9. Paull, C.K.; Dillon, W.P. (Eds.) *Natural Gas Hydrates: Occurrence, Distribution, and Detection*; Geophysical Monograph Series; American Geophysical Union: Washington DC, USA, 2001; Volume 124.
10. Claypool, G.E.; Kaplan, I.R. The Origin and Distribution of Methane in Marine Sediments. In *Natural Gases in Marine Sediments*; Kaplan, I.R., Ed.; Springer: Berlin/Heidelberg, Germany, 1974; pp. 99–139.
11. Alexei, V.M. Molecular and stable isotope compositions of natural gas hydrates: A revised global dataset and basic interpretations in the context of geological settings. *Org. Geochem.* **2005**, *36*, 681–702.
12. Wallmann, K.; Pinero, E.; Burwicz, E.; Haeckel, M.; Hensen, C.; Dale, A.W.; Ruppel, C. The Global Inventory of Methane Hydrate in Marine Sediments: A Theoretical Approach. *Energies* **2012**, *5*, 2449–2498. [[CrossRef](#)]
13. Pinero, E.; Marquardt, M.; Hensen, C.; Haeckel, M.; Wallmann, K. Estimation of the global inventory of methane hydrates in marine sediments using transfer functions. *Biogeosciences* **2013**, *10*, 959–975. [[CrossRef](#)]
14. Ruppel, C.; Kessler, J.D. The interaction of climate change and methane hydrates. *Rev. Geophys.* **2017**, *55*, 126–168. [[CrossRef](#)]
15. Alexei, V.M. Global estimates of hydrate-bound gas in marine sediments: How much is really out there? *Earth Sci. Rev.* **2004**, *66*, 183–197.
16. Boswell, R.; Collett, T.S. Current perspectives on gas hydrate resources. *Energy Environ. Sci.* **2011**, *4*, 1206–1215. [[CrossRef](#)]
17. Collett, T.; Johnson, A.; Knapp, C.; Boswell, R. *Natural Gas Hydrates—Energy Resource Potential and Associated Geologic Hazards*; AAPG Memoir, 89; American Association of Petroleum Geologists: Tulsa, OK, USA; Department of Energy, National Energy Technology Laboratory: Albany, OR, USA; AAPG Foundation: Tulsa, OK, USA; AAPG Energy Minerals Division: Tulsa, OK, USA, 2010.
18. Makogon, Y.; Holditch, S.; Makogon, T. Natural gas-hydrates—A potential energy source for the 21st Century. *J. Pet. Sci. Eng.* **2007**, *56*, 14–31. [[CrossRef](#)]
19. Max, M.D.; Johnson, A.H.; Dillon, W.P. *Economic Geology of Natural Gas Hydrate*; Springer: Dordrecht, The Netherlands, 2006.
20. Collett, T.S.; Boswell, R.; Cochran, J.R.; Kumar, P.; Lall, M.; Mazumdar, A.; Ramana, M.V.; Ramprasad, T.; Riedel, M.; Sain, K.; et al. Geologic implications of gas hydrates in the offshore of India: Results of the National Gas Hydrate Program Expedition 01. *Mar. Pet. Geol.* **2014**, *58*, 3–28. [[CrossRef](#)]
21. Konno, Y.; Fujii, T.; Sato, A.; Akamine, K.; Naiki, M.; Masuda, Y.; Yamamoto, K.; Nagao, J. Key Findings of the World’s First Offshore Methane Hydrate Production Test off the Coast of Japan: Toward Future Commercial Production. *Energy Fuels* **2017**, *31*, 2607–2616. [[CrossRef](#)]
22. Zhang, W.; Liang, J.; Wei, J.; Lu, J.; Su, P.; Lin, L.; Huang, W.; Guo, Y.; Deng, W.; Yang, X.; et al. Geological and geophysical features of and controls on occurrence and accumulation of gas hydrates in the first offshore gas-hydrate production test region in the Shenhu area, Northern South China Sea. *Mar. Pet. Geol.* **2020**, *114*, 104191. [[CrossRef](#)]
23. Minshull, T.A.; Westbrook, G.K.; Weitemeyer, K.A.; Sinha, M.C.; Goswami, B.K.; Marsset, B. Leaking methane reservoirs offshore Svalbard. *Eos Trans. Am. Geophys. Union* **2012**, *93*, 413–414. [[CrossRef](#)]
24. Liu, L.; Ryu, B.; Sun, Z.; Wu, N.; Cao, H.; Geng, W.; Zhang, X.; Jia, Y.; Xu, C.; Guo, L.; et al. Monitoring and research on environmental impacts related to marine natural gas hydrates: Review and future perspective. *J. Nat. Gas Sci. Eng.* **2019**, *65*, 82–107. [[CrossRef](#)]
25. Kvenvolden, K.A. Gas hydrates-geological perspective and global change. *Rev. Geophys.* **1993**, *31*, 173–187. [[CrossRef](#)]
26. Waite, W.F.; Santamarina, J.C.; Cortes, D.D.; Dugan, B.; Espinoza, D.N.; Germaine, J.; Jang, J.; Jung, J.W.; Kneafsey, T.J.; Shin, H.; et al. Physical properties of hydrate-bearing sediments. *Rev. Geophys.* **2009**, *47*. [[CrossRef](#)]
27. Maslin, M.; Owen, M.J.; Betts, R.; Day, S.; Jones, T.D.; Ridgwell, A. Gas hydrates: Past and future geohazard? *Philos. Trans. R. Soc. A* **2010**, *368*, 2369–2393. [[CrossRef](#)] [[PubMed](#)]
28. Sultan, N.; Ruffine, L.; Garziglia, S.; Ker, S.; Vanneste, M.; Humphrey, G.D. Seabed Gas Hydrates. In *Encyclopedia of Maritime and Offshore Engineering*; John Wiley & Sons: Hoboken, NJ, USA, 2018; pp. 1–12.

29. Yeliseti, S.; Spence, G.D.; Riedel, M. Role of gas hydrates in slope failure on frontal ridge of northern Cascadia margin. *Geophys. J. Int.* **2014**, *199*, 441–458. [[CrossRef](#)]
30. Carroll, J.J. *Natural Gas Hydrates; A Guide for Engineers*; Gulf Professional Publishing: Houston, TX, USA, 2009; p. 248.
31. Marinhas, S.; Delahaye, A.; Fournaison, L.; Dalmazzone, D.; Fürst, W.; Petitet, J.P. Modelling of the available latent heat of a CO₂ hydrate slurry in an experimental loop applied to secondary refrigeration. *Chem. Eng. Process. Process. Intensif.* **2006**, *45*, 184–192. [[CrossRef](#)]
32. Li, G.; Hwang, Y.; Radermacher, R. Review of cold storage materials for air conditioning application. *Int. J. Refrig.* **2012**, *35*, 2053–2077. [[CrossRef](#)]
33. Wang, X.; Dennis, M.; Hou, L. Clathrate hydrate technology for cold storage in air conditioning systems. *Renew. Sustain. Energy Rev.* **2014**, *36*, 34–51. [[CrossRef](#)]
34. Cheng, C.; Wang, F.; Tian, Y.; Wu, X.; Zheng, J.; Zhang, J.; Li, L.; Yang, P.; Zhao, J. Review and prospects of hydrate cold storage technology. *Renew. Sustain. Energy Rev.* **2020**, *117*, 109492. [[CrossRef](#)]
35. Linga, P.; Daraboina, N.; Ripmeester, J.; Englezos, P. Enhanced rate of gas hydrate formation in a fixed bed column filled with sand compared to a stirred vessel. *Chem. Eng. Sci.* **2012**, *68*, 617–623. [[CrossRef](#)]
36. Liu, H.; Zhan, S.; Guo, P.; Fan, S.; Zhang, S. Understanding the characteristic of methane hydrate equilibrium in materials and its potential application. *Chem. Eng. J.* **2018**, *349*, 775–781. [[CrossRef](#)]
37. Liu, Z.; Pan, Z.; Zhang, Z.; Liu, P.; Shang, L.; Li, B. Effect of Porous Media and Sodium Dodecyl Sulphate Complex System on Methane Hydrate Formation. *Energy Fuels* **2018**, *32*, 5736–5749. [[CrossRef](#)]
38. Wang, J.; Zhao, J.; Zhang, Y.; Wang, D.; Li, Y.; Song, Y. Analysis of the effect of particle size on permeability in hydrate-bearing porous media using pore network models combined with CT. *Fuel* **2016**, *163*, 34–40. [[CrossRef](#)]
39. Lu, H.; Kawasaki, T.; Ukita, T.; Moudrakovski, I.; Fujii, T.; Noguchi, S.; Shimada, T.; Nakamizu, M.; Ripmeester, J.; Ratcliffe, C. Particle size effect on the saturation of methane hydrate in sediments—Constrained from experimental results. *Mar. Pet. Geol.* **2011**, *28*, 1801–1805. [[CrossRef](#)]
40. Ge, B.B.; Zhong, D.L.; Lu, Y. Influence of water saturation and particle size on methane hydrate formation and dissociation in a fixed bed of silica sand. *Energy Procedia* **2019**, *158*, 5402–5407. [[CrossRef](#)]
41. Heeschen, K.U.; Schicks, J.M.; Oeltzschner, G. The promoting effect of natural sand on methane hydrate formation: Grain sizes and mineral composition. *Fuel* **2016**, *181*, 139–147. [[CrossRef](#)]
42. Prasad, P.S.; Chari, V.D.; Sharma, D.V.; Murthy, S.R. Effect of silica particles on the stability of methane hydrates. *Fluid Phase Equilibria* **2012**, *318*, 110–114. [[CrossRef](#)]
43. Bagherzadeh, S.A.; Moudrakovski, I.; Ripmeester, J.A.; Englezos, P. Magnetic Resonance Imaging of Gas Hydrate Formation in a Bed of Silica Sand Particles. *Energy Fuels* **2011**, *25*, 3083–3092. [[CrossRef](#)]
44. Kumar, A.; Sakpal, T.; Roy, S.; Kumar, R. Methane hydrate formation in a test sediment of sand and clay at various levels of water saturation. *Can. J. Chem.* **2015**, *93*, 874–881. [[CrossRef](#)]
45. Ruffine, L. Exploring methane-hydrate formation and dissociation in geologic materials through laboratory experiments: Kinetic behavior and morphology. *Fuel* **2015**, *141*, 173–184. [[CrossRef](#)]
46. Circone, S.; Kirby, S.H.; Stern, L.A. Direct Measurement of Methane Hydrate Composition along the Hydrate Equilibrium Boundary. *J. Phys. Chem. B* **2005**, *109*, 9468–9475. [[CrossRef](#)]
47. Glew, D.N. Aqueous solubility and the gas-hydrates. The methane-water system1. *J. Phys. Chem.* **1962**, *66*, 605–609. [[CrossRef](#)]
48. Wang, P.; Wang, S.; Song, Y.; Yang, M. Dynamic measurements of methane hydrate formation/dissociation in different gas flow direction. *Appl. Energy* **2018**, *227*, 703–709. [[CrossRef](#)]
49. Song, Y.; Wang, P.; Jiang, L.; Zhao, Y.; Yang, M. Methane hydrate formation/reformation in three experimental modes: A preliminary investigation of blockage prevention during exploitation. *J. Nat. Gas Sci. Eng.* **2015**, *27*, 1814–1820. [[CrossRef](#)]
50. Hazen, A. *Some Physical Properties of Sand and Gravel, with Special Reference to Their Use in Filtration*; 24th Annual Report; State Board of Health: Boston, MA, USA, 1892; pp. 539–556.
51. Ren, X.; Santamarina, J. The hydraulic conductivity of sediments: A pore size perspective. *Eng. Geol.* **2018**, *233*, 48–54. [[CrossRef](#)]
52. Rosas, J.; Lopez, O.; Missimer, T.M.; Coulibaly, K.; Dehwah, A.H.; Sesler, K.; Lujan, L.; Mantilla, D. Determination of hydraulic conductivity from grain-size distribution for different depositional environments. *Groundwater* **2014**, *52*, 399–413. [[CrossRef](#)] [[PubMed](#)]

53. Santamarina, J.C.; Klein, K.A.; Wang, Y.H.; Prencke, E. Specific surface: Determination and relevance. *Can. Geotech. J.* **2002**, *39*, 233–241. [[CrossRef](#)]
54. Taylor, D.W. Fundamentals of Soil Mechanics. *Soil Sci.* **1948**, *66*, 161. [[CrossRef](#)]
55. Ripmeester, J.; Alavi, S. Some current challenges in clathrate hydrate science: Nucleation, decomposition and the memory effect. *Curr. Opin. Solid State Mater. Sci.* **2016**, *20*, 344–351. [[CrossRef](#)]
56. Veluswamy, H.P.; Kumar, S.; Kumar, R.; Rangsunvigit, P.; Linga, P. Enhanced clathrate hydrate formation kinetics at near ambient temperatures and moderate pressures: Application to natural gas storage. *Fuel* **2016**, *182*, 907–919. [[CrossRef](#)]
57. Fandiño, O.; Ruffine, L. Methane hydrate nucleation and growth from the bulk phase: Further insights into their mechanisms. *Fuel* **2014**, *117*, 442–449. [[CrossRef](#)]
58. Chen, X.; Espinoza, D.N. Surface area controls gas hydrate dissociation kinetics in porous media. *Fuel* **2018**, *234*, 358–363. [[CrossRef](#)]
59. Hassanpouryouzband, A.; Joonaki, E.; Vasheghani Farahani, M.; Takeya, S.; Ruppel, C.; Yang, J.; English, N.J.; Schicks, J.M.; Edlmann, K.; Mehrabian, H.; et al. Gas hydrates in sustainable chemistry. *Chem. Soc. Rev.* **2020**, *49*, 5225–5309. [[CrossRef](#)]
60. Wang, S.; Yang, M.; Liu, W.; Zhao, J.; Song, Y. Investigation on the induction time of methane hydrate formation in porous media under quiescent conditions. *J. Pet. Sci. Eng.* **2016**, *145*, 565–572. [[CrossRef](#)]



© 2020 by the authors. Licensee MDPI, Basel, Switzerland. This article is an open access article distributed under the terms and conditions of the Creative Commons Attribution (CC BY) license (<http://creativecommons.org/licenses/by/4.0/>).